ACS APPLIED MATERIALS & INTERFACES

Research Article

www.acsami.org

# High-Efficiency Plasmon-Enhanced and Graphene-Supported Semiconductor/Metal Core–Satellite Hetero-Nanocrystal Photocatalysts for Visible-Light Dye Photodegradation and $H_2$ Production from Water

Jie Zhang, Ping Wang, Jian Sun, and Yongdong Jin*

State Key Laboratory of Electroanalytical Chemistry, Changchun Institute of Applied Chemistry, Chinese Academy of Sciences, Changchun, Jilin 130022, P. R. China

Supporting Information

**ABSTRACT:** Solar-driven photocatalytic process based on electron–hole pair production in semiconductors is a long sought-after solution to a green and renewable energy and has attracted a renaissance of interest recently. The relatively low photocatalytic efficiency, however, is a main obstacle to their practical applications. A promising attempt to solve this problem is by combined use of metal nanoparticles, by taking advantage of strong and localized plasmonic near-field to enhance solar absorption and to increase the electron–hole pair generation rate at the surface of semiconductor. Here, we report a semiconductor/metal visible-light photocatalyst based on CdSe/CdS-Au (QD-Au) core–satellite heteronanocrystals, and assemble them on graphene nanosheets for better photocatalytic reaction. The as-synthesized photocatalyst exhibits excellent plasmon-enhanced photocatalytic activities toward both photodegradation of organic dye and visible-light $H_2$ generation from water. The $H_2$ evolution rate achieves a maximum of 3113 $\mu$mol $h^{-1}$ $g^{-1}$ for the heteronanocrystal-graphene composites, which is about 155% enhancement compared to nonplasmonic QD-G sample and 340% enhancement compared to control QD-Au-G sample, and the apparent quantum efficiency (QE) reaches to 25.4% at wavelength of 450 nm.

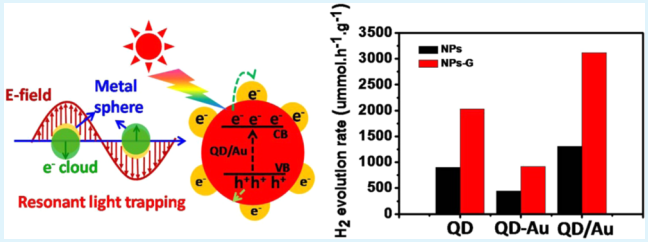


**KEYWORDS:** *semiconductor nanocrystal, plasmon enhancement, graphene, photocatalysis, $H_2$ generation*

## 1. INTRODUCTION

Semiconductor photocatalysis, especially that based on nanoscale materials, has been envisioned as a viable strategy for simultaneously solving the incoming energy and environmental problems since the discovery of photocatalytic water splitting by using $TiO_2$ electrodes in 1972.[1−7] To date, photocatalytic nanosystems are based mostly on oxide semiconductors (such as $TiO_2$, ZnO, etc.) and operated with UV light,[8−10] which accounts for only a small fraction of the incident sunlight (~4%). Additionally, the limitation in synthetic chemistry of oxide semiconductor also limits its further practical applications in the field of photocatalysis.

Recently, researchers have switched their efforts to develop visible-light-responsive photocatalysts because 43% of the solar energy is the visible light.[11−13]Among other candidates, quantum-sized semiconductor nanocrystals (S-NCs) are promising alternative materials for light driven proton reduction due to their unique properties.[14,15] Meanwhile, enormous progress made on the synthetic chemistry of various semiconductor NCs (the size and morphology control, band gap and composition engineering, and so on) benefits photocatalyst materials design.[16−18] However, a drawback of the S-NC photocatalytic systems is that the photogenerated electrons and holes arising from the excited states of S-NCs are unstable and can easily recombine, which results in low photocatalytic efficiency.[2,3,14] Various strategies have been employed to improve the carrier separation efficiency of semiconductor photocatalysts,[4,8,15,19−24] such as depositing noble metals on semiconductor NCs, synthesis of heterogeneous semiconductors, and incorporation of semiconductor particles with carbon materials (e.g., graphene, carbon nanotube). Especially, anisotropic multicomponent nanomaterials (different metals and semiconductors) composed of graphene nanosheets (GNS) are highly desirable in the field of photocatalysis because of their ability to tune the charge separation behavior through the interaction between them by their favorable band alignment.[4,14] Previously, however, the discrete S-NCs and noble metal NPs, of which platinum and palladium were usually used,[3,4,14] were loaded on the surface of GNS via different ways with indirect contacts, which lows the separation efficiency of photogenerated carriers.[14,19] Some plasmonic and nonplasmonic noble metal–semiconductor hybrid nanostructures have been recently synthesized and applied to photocatalytic reactions, and compared with

Received: August 10, 2014
Accepted: November 4, 2014
Published: November 4, 2014

  

nonplasmonic noble metal−semiconductor photocatalytic materials, the plasmonic hybrid nanomaterials displayed better photocatalytic activity because they can increase the light absorption,[24−30] but there are few reports about graphene-supported plasmonic metal−semiconductor hybrid photocatalytic nanomaterials, so it is very necessary and helpful to study plasmon-induced carrier behavior and photocatalytic activity of the graphene-supported semiconductor/metal heteronanocrystal materials. Designing and preparing structurally well-defined and graphene-supported semiconductor/metal heteronanocrystals (HNCs) with high photocatalytical performance is therefore highly desired and remains a great challenge.

Here, we report a novel semiconductor/metal HNC photocatalyst based on CdSe/CdS-Au core−satellite HNCs and their assembly on GNS for visible-light dye photodegradation and $H_2$ production from water. Direct contact between satellite Au NPs and core S-NC is designed to trap plasmonically visible light and form a localized electromagnetic energy close to the surfaces of the S-NC, which increases the electron−hole pair generation rate of the nanosystem. The photocatalytic results prove that the as-prepared CdSe/CdS/Au-graphene (QD/Au-G) composites have a significantly better photocatalytic performances as compared with the nonplasmonic CdSe/CdS-graphene (QD-G) and semiconductor-Au indirect contacted control QD-Au-G composites for photodegradation of organic dyes and water splitting.

## 2. EXPERIMENTAL SECTION

**Materials.** Cadmium oxide (99.99%), selenium (99.5%, 100 mesh), sulfur (99.98%, powder), trioctylphosphine (TOP, 90%), 1-octadecene (ODE), oleic acid (OA, 90%), oleylamine (OLA, 70%), and octadecylamine (ODA, 97%) were purchased from Aldrich. Dodecylamine (DDA, 99%) was obtained from Aladdin. $HAuCl_4$, $Na_2S$, $Na_2SO_3$, and all organic solvents were purchased from Beijing chemical works. All chemicals were used directly without any further purification.

**Synthesis of CdSe/CdS Nanocrystals.** The CdSe/CdS core/shell NCs were synthesized by SILAR technique as reported in literature. A typical SILAR synthesis was performed as follows: 4 mL of ODE and 1.5 g of ODA were loaded into a 50 mL reaction vessel, heated to 100 °C under vacuum for 1 h, and cooled to room temperature. The CdSe NCs in hexane (3.9 nm in diameter, $2.9 \times 10^{-7}$ mol) were added, and the system was kept at 100 °C under vacuum for 30 min to remove the hexane and other undesired materials of low vapor pressure. Subsequently, the solution was heated to 235 °C under $N_2$-flow where the shell growth was performed. This is followed by alternating addition of Cd precursors and sulfur precursors, respectively, the amount of which was calculated from the respective volumes of concentric spherical shells with a thickness of one hypothetical monolayer (ML). A period of 15 min between each addition was sufficient for the reaction to be completed. The complete coverage procedure of CdSe cores with 6 MLs of CdS took about 3 h in total. After this time, the solution was kept for another 30 min at 260 °C and finally cooled to room temperature. For purification, 10 mL of hexane was added and the unreacted compounds and byproducts were removed by successive methanol extraction (at least three times) until the methanol phase was clear.

Photoluminescence quantum yields (QYs) of the nanocrystals was determined from the integrated fluorescence intensity of the nanocrystals and the reference (R6G, excited at 488 nm, emission at 580 nm, QY = 95%)

$$QY_s = (F_s A_r QY_r)/(F_r A_s) \quad (1)$$

Where $F_s$ and $F_r$ are the integrated fluorescence emissions of the sample and the reference, $A_s$ and $A_r$ are the absorbance of the sample and the reference at the excitation wavelength, and $QY_s$ and $QY_r$ are the quantum yields of the sample and the reference, respectively.

**Deposition of Au on Colloidal CdSe/CdSCore/Shell Nanocrystals.** For the synthesis of heterogeneous semiconductor/metal hybrids, 5 mL of preformed CdSe/CdS core/shell NCs in toluene were mixed with 5 mL of 10 mM$HAuCl_4$ precursor solution in toluene. The mixture was aged for 1 h. Additional reducing agent was not necessary; DDA could reduce the gold ions in toluene sufficiently at room temperature in the presence of semiconductor NCs.

**Graphene (G) Synthesis.** The single sheet of graphite oxide (GO) was synthesized from natural graphite powder by exfoliation of GO under ultrasonication in DMF according to the literature. The DMF dispersion of GO (0.5 mg/mL) was heated to refluxing for 6 h and cooled to room temperature to convert GO to G.

**Synthesis of CdSe/CdS/Au-G Composite.** Fifteen milligrams of CdSe/CdS/Au HNCs dispersed in 10 mL of hexane was added into 10 mL of $H_2O$ solution of graphene (0.5 mg/mL) and the mixture was stirred for 1 h. Ten milliliters of ethanol was then added and the precipitate was separated from the solvents by centrifuging for 10 min at 9500 rpm, the as-prepared CdSe/CdS/Au-G sample was washed by ethanol three times for removing the surface ligands of CdSe/CdS/Au and make the CdSe/CdS/Au direct contact with graphene nanosheets. The CdSe/CdS/Au-G composites were dried under ambient conditions for further use.

**Characterizations.** TEM, high resolution TEM (HRTEM), corresponding TEM element mapping and energy-dispersive spectrometry (EDS) measurements were carried out by using a FEI TECNAI F20 EM with an accelerating voltage of 200 kV equipped with an energy dispersive spectrometer. XPS measurements were performed with Thermo ESCALAB VG Scientific 250 and equipped with monochromatized Al Ka excitation. The fluorescence intensity (FL) spectra were recorded by a PerkinElmer LS-55 Luminescence Spectrometer (PerkinElmer Instruments U.K.). UV−vis absorption spectra were recorded by a UV 2100 Shimadzu spectrophotometer using a 1 cm path length quartz cell at room temperature. Photocurrents were measured using an electrochemical analyzer (CHI832C Instruments) with a standard three-electrode system using the prepared samples as the working electrodes with an active area of ca. 1.44 $cm^2$, a Pt wire as the counter electrode, and Ag/AgCl (saturated KCl) as a reference electrode.

**Photocatalytic Experiments.** Typically, an aqueous solution of the MB and RDB dyes (0.01 g/L, 10 mL) and the photocatalysts (QD-G, QD-Au-G, QD/Au-G, 5 mg each) were placed in a 20 mL cylindrical quartz vessel, and then the solution was first stirred 30 min in the dark to achieve an adsorption and desorption equilibrium of dyes on the catalyst surface. The photoreaction container was exposed to the visible light irradiation by a 300 W xenon lamp and a cutoff filter equipped as the light source (>420 nm), which was positioned 30 cm away from the vessel. At 10 min intervals, the reacted solution was analyzed by a UV−visible spectrophotometer (UV 2100, Shimadzu). The degree of degradation was expressed by $C/C_o$, which is the ratio of the temporal dyes concentration to the initial dyes concentration after absorption equilibrium in the dark. In the durability test of QD/Au-G catalyst in the photodegradation of MB under visible light, four consecutive cycles were tested. At the beginning, 5 mg of QD/Au-G was dispersed in 10 mL of MB solution (0.01g/mL). Then the mixture underwent four consecutive cycles, each lasting for 60 min. After each cycle, the catalyst was filtrated and washed thoroughly with water, and then fresh MB solution (0.01g/mL) was added to the catalyst.

The photocatalytic water splitting experiments were operated in a 100 mL cylindrical quartz flask, the openings of which were sealed with a silicone rubber septum and Quartz glass cover, at ambient temperature and atmospheric pressure. A 300 W xenon arc lamp with a UV-cutoff filter (>420 nm) was used as a visible light source to carry out the photocatalytic reaction and was positioned 20 cm away from the reactor. In a typical experiment, 50 mg of the as-prepared QD/Au-G photocatalyst was dispersed with constant stirring in 50 mL solution water containing 0.35 M $Na_2S$ and 0.25 M $Na_2SO_3$ as holes scavenger. Before beginning the photocatalytic reaction, the system was then pumped down at room temperature with a mechanical pump

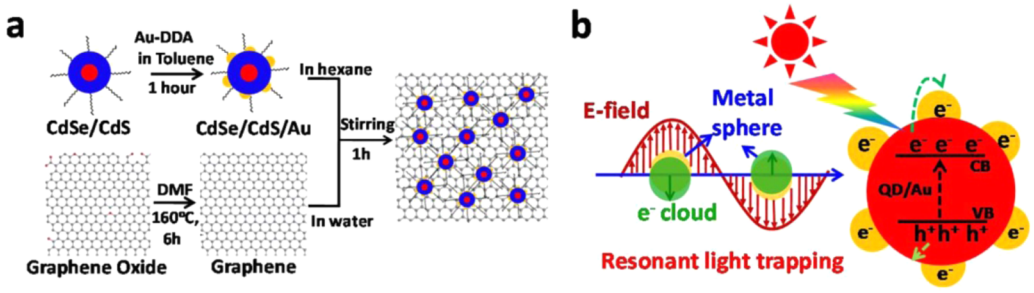


**Figure 1.** Preparation and photocatalytic mechanisms of the semiconductor/metal core−satellite HNC. (a) Schematic illustration of the preparation of CdSe/CdS-Au (QD/Au) core−satellite HNCs and their assembly on reduced graphene nanosheets. (b) The charge separation and transfer process of the QD/Au HNCs by the localized SPR effect.

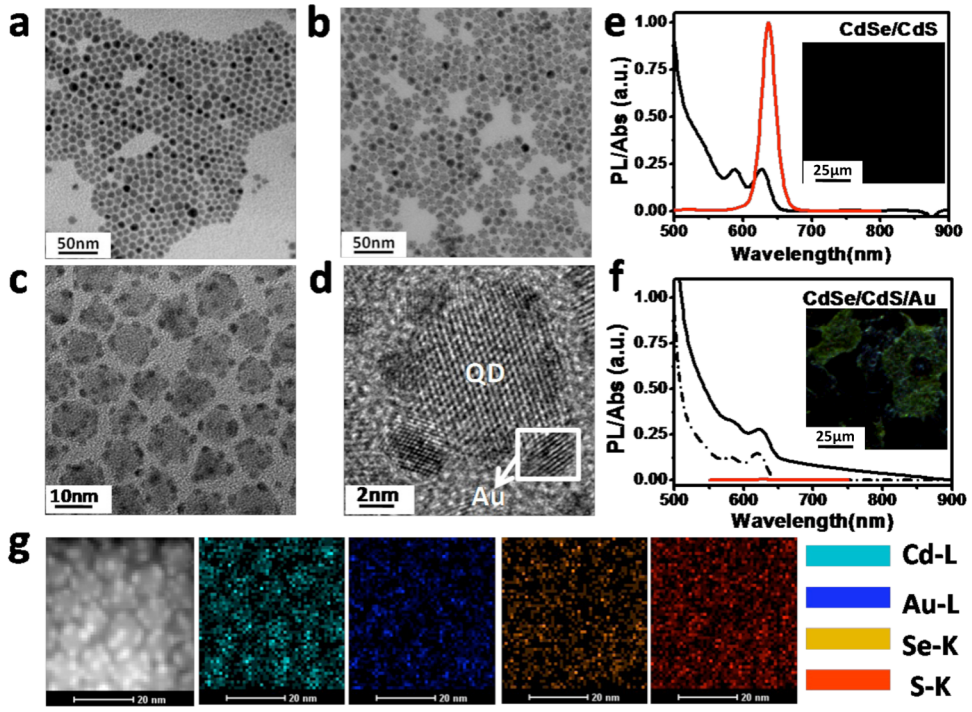


**Figure 2.** TEM and optical properties of the CdSe/CdS-Au core−satellite HNCs. The TEM images of (a) original CdSe/CdS core/shell and (b, c) as-prepared CdSe/CdS-Au HNCs, (d) HRTEM image of the CdSe/CdS-Au HNCs. The UV−vis (black), PL (red) spectra, and dark-field scattering images (inset) of the (e) CdSe/CdS QDs, and (f) CdSe/CdS-Au HNCs. (g) STEM images and mapping analysis of the CdSe/CdS-Au HNCs.

for 30 min to remove the dissolved oxygen. During the whole reduction process, agitation of the solution ensured uniform irradiation of the QD/Au-G suspension. A 0.4 mL sample of the generated gas was collected intermittently through the septum, and hydrogen content was analyzed by gas chromatograph (GC-2014C, Shimadzu, Japan, TCD, argon as a carrier gas and 5 Å molecular sieve column). All glassware was rigorously cleaned and carefully rinsed with distilled water prior to use.

The apparent quantum efficiency (QE) was measured under the same photocatalytic reaction condition. A 300 W xenon arc lamp with a UV-band-pass filter (450 nm) were used as light sources to trigger the photocatalytic reaction, and the intensity and number of photons of the light source at 450 nm were measured by UV−visible spectrophotometry. Typically, 50 mL (0.01M) $K_3Fe(C_2O_4)_3.3H_2O$ solution ($V_0$) were placed in cylindrical quartz flask under stirring, and then the solution were irradiated 20s using 450 nm light, 5 mL samples ($V_1$) were taken and added into a 50 mL brown volumetric flask; 10 mL of (0.01M)1,10-Phenanthroline monohydrate solution and 10 mL of acetic acid-sodium acetate buffer solution (pH 4.6) were then added, diluted to 50 mL ($V_2$), and placed flask in the dark for 30 min.Three parallel samples of each were taken for measuring, and then the absorbance was measured at 510 nm ($A_t$). The QE was finally calculated according to Eq2.

$$QE = 2nN/n'St \quad (2)$$

where $n$ is the amount of hydrogen generated in $t$ time (mol); $N$, Avogadro's constant; $n'$, the number of light source emitted photon in per unit area and per unit time ($s^{-1}$ $m^{-2}$); and $S$, the area of light source emitted reaction liquid ($m^2$).

$$n' = (A_t - A_0)V_2V_0N/\varepsilon l V_1 \Phi_{Fe}{}^{2+} t \quad (3)$$

where $A_0$ is the absorbance of zero irradiation time; $\varepsilon$, the molar extinction coefficient of $Fe^{2+}$; $l$, the thickness of the cuvette; $t$ is the irradiation time of the light source, $\Phi_{Fe}{}^{2+} = 1.11$ ($\lambda$ = 450 nm).

## 3. RESULTS AND DISCUSSION

Figure 1a briefly illustrates the preparation of CdSe/CdS-Au (QD/Au) core−satellite HNCs and their assembly on GNS. The CdSe/CdS core/shell NCs were synthesized by previously reported SILAR technique.[31] We chose CdSe/CdS core/shell NCs rather than CdSe or CdS NCs as the visible-light HNC photocatalyst's semiconductor component because of their

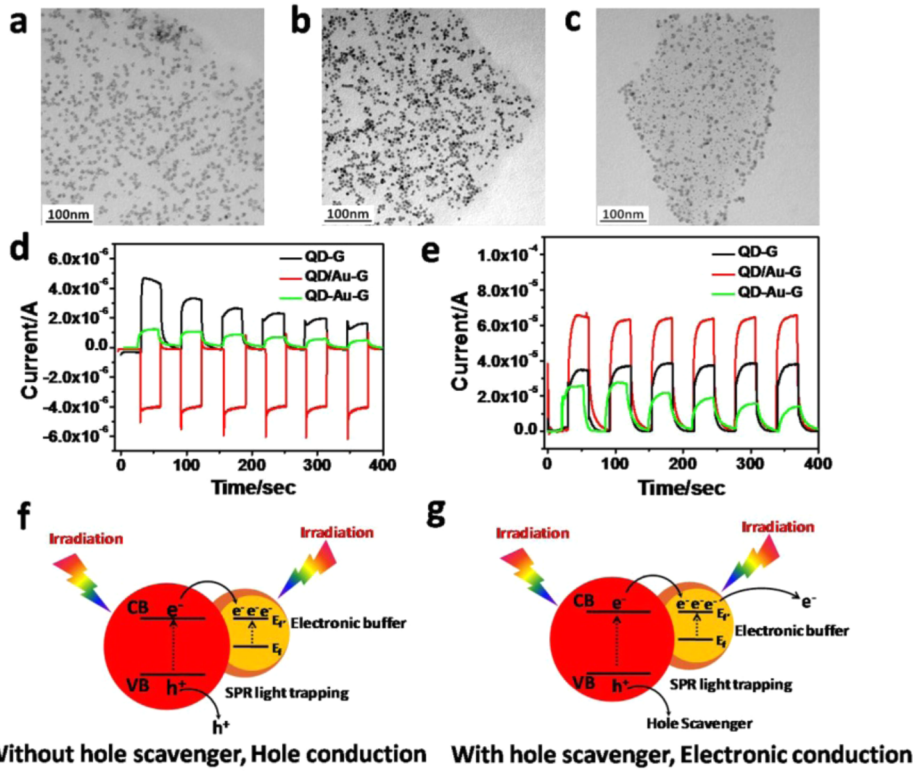


**Figure 3.** TEM, photocurrent responses, and carrier transfer process of the composite QD/Au-G photocatalyst. (a–c) The TEM images of the QD/Au HNC-G, QD-G, and QD-Au-G, respectively.(d) The photocurrent response of the QD-G (black), QD/Au HNC-G (red), and QD-Au-G (green), respectively, under visible light using $NaNO_3$ (0.1M) as electrolyte solution. (e) The photocurrent response of the QD-G (black), QD/Au HNC-G (red), and QD-Au-G (green), respectively, under visible light using $Na_2S$ (0.1 M) and $Na_2SO_3$ (0.02 M) as electrolyte solution. (f, g) Photoinduced transfer processes of carriers in the QD/Au HNC-G Composites using different electrolyte solution: (f) $NaNO_3$ (0.1 M), non hole scavenger; (g) $Na_2S$ (0.1 M) + $Na_2SO_3$ (0.02 M), hole scavenger.

higher photocorrosion resistance and better photostability;[32,33] meanwhile, the outer CdS-shell can effectively passivate the surface-deep traps of CdSe NCs, which maintains the photogenerated electrons at a sufficient reduction potential to reduce water.[33] More importantly, the core/shell configuration is thought to help sequester high-energy electrons to facilitate $H_2$ photogeneration because the photoexcited electrons must tunnel through the CdS-shell and initiate redox chemistry on the surface, which does not adversely hinder photoactivity because the redox time scale is significantly longer than the tunneling time scale.[33] Small satellite Au NPs were prepared by Au deposition on the surface of CdSe/CdS NCs by aging the mixture of QDs and Au(3+)-dodecylamine (DDA) precursor in toluene for 1 h. Extra reducing agent was not necessary in the reaction system since DDA could reduce $Au^{3+}$ sufficiently in the presence of S-NCs.[34] It is impossible to prepare QD/Au core/shell nanocrystals by our experiment method, although we increase the amount of Au precursor during the preparation, the as-prepared nanoparticles are still core–satellite heterostructure nanocrystals but not QD/Au core/shell structure. The complexation of QD/Au HNCs with graphene (prepared by dimethylformamide (DMF) reduction of graphene oxide at ~150 °C,[35] and confirmed by XPS characterization (see Figure S1 in the Supporting Information) can be completed by mixing QD/Au in hexane with the aqueous graphene solution.[36] Figure 1b depicts the localized surface plasmon resonance (LSPR) effect on charge separation and transfer process of QD/Au HNCs. Under visible-light irradiation, the satellite Au NPs form a localized electromagnetic energy close to the surfaces of the QD, in which the plasmon-exciton interaction allows for the selective formation of electron/hole ($e^-/h^+$) pairs in the near-surface region of the semiconductor.[25,26] During the process, electrons are excited from the valence band (VB) to the conduction band (CB) of the QD and then transfer to Au NPs, the Au NPs as electron buffer store electrons, which leads to the Fermi level of the HNC shifting close to the CB of the QD; meanwhile, the holes are left on the surface of QD.[37] All of these will benefit potential photocatalytic applications.

Figure 2a shows typical TEM image of the monodispersed organic CdSe/CdS NCs used, with diameter of ~9.2 nm and organized in 2D superlattices. TEM images of the as-prepared QD/Au HNCs (Figure 2b, c) show that the small Au NPs with average diameter of ~2 nm are uniformly deposited on the surface of QD to form a core–satellite nanostructure. Because of strong contrast, it is clearly seen that each QD particle is decorated by ~6–12 small Au NPs. Similarly, the as-prepared uniform organic QD/Au HNCs formed spontaneously well-ordered 2D superlattices. HRTEM image of a single QD/Au HNC (Figure 2d) reveals a high crystallinity with continuous lattice fringes throughout the whole particle. We can clearly observe the CdS (002) lattice of the QD in the center and the Au (111) lattice in the edges simultaneously by adjusting imaging conditions. The elemental mapping (Figure 2g) and energy-dispersive X-ray (see Figure S2 in the Supporting Information) analyses further confirmed the chemical nature of the HNCs.

Next, we thoroughly characterized the optical properties of the QDs before and after Au deposition to study the effect of

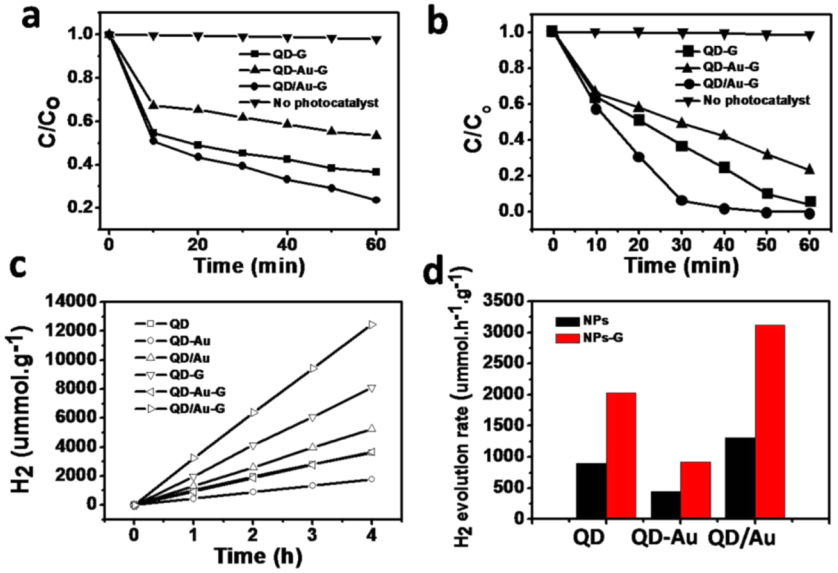


**Figure 4.** Photocatalytic applications of the composite QD/Au-G photocatalyst. (a, b) Photodegradation of methylene blue ($2.7 \times 10^{-5}$ M,10 mL) and rhodamine B (0.01 g/mL) under visible light (>420 nm) over QD/Au-G, QD-G, and QD-Au-G photocatalysts (3 mg), respectively. (c) Comparison of the visible-light photocatalytic activity of the samples QD/Au, QD, QD-Au, and their graphene composites (QD/Au-G, QD-G, QD-Au-G) for the $H_2$ production using an aqueous solution containing 0.35 M $Na_2S$ and 0.25 M $Na_2SO_3$ as a sacrificial reagent, a 300 W xenon arc lamp was used as the light source. (d) $H_2$ production rate of the QD/Au, QD, and QD-Au and their graphene composites (QD/Au-G, QD-G, QD-Au-G).

Au NP growth on the QD's optical properties. As shown in Figure 2e, the CdSe/CdS QDs absorbed over a broad spectrum with increasing molar extinction coefficient toward shorter wavelengths and a first quantum confinement peak of 620 nm, almost cover the entire ultraviolet−visible light region, which means we can use most of the solar radiation energy for photocatalytic reaction. The QDs have good photoluminescence (PL) properties and their emission peak centered at 639 nm. The quantum yield (QY) of the QDs was calculated to be ∼70%, which is high and attributed to the passivation of surface-deep traps via the outer CdS-shell. After satellite Au NPs formation, the optical spectra of the resultant QD/Au HNCs showed distinct change. As shown in Figure 2f, although absorption spectra of the QD/Au HNCs (solid line) showed similar profile as the QDs, the absorption intensity increased greatly than that of the QDs of same concentration (dotted line), with a pronounced raised absorption tail toward longer wavelengths. This is a strong reflection of spectral overlapping of the QDs and the decorated Au NPs; the otherwise weak LSPR peaks of the small Au NPs (∼2 nm) centered at ∼508 nm and ∼600−700 nm due to collective resonance of closely packed satellite Au NPs, was buried by the strong QD absorption in this region. But the pronounced dark-field scattering imaging of the green-yellow colored QD/Au HNCs (as shown in the inset of Figure 2f), and FDTD simulation calculation (see Figure S3 in the Supporting Information) proved plasmonic nature of the resultant QD/Au HNCs, which can increase the visible light absorption and will benefit for photocatalytic applications. Differing from our previously reported polymer-gaped QD/Au core/shell NPs with significantly maintained PL,[38] a strong quenching of the QD PL was observed and as expected, after the direct Au deposition on QD's surface to form QD/Au HNCs (red line in Figure 2f). The quenching is expected via a nonradiative pathway created by the proximity of Au, leading to electron transfer from the QD to Au.[19] This is highly desirable for photocatalytic purpose that involves electron transfer process. Control experiments by simply mixing discrete core QDs and Au NPs of similar size did not reproduce the observed absorption and the PL of QD almost remained (see Figure S4 in the Supporting Information). We therefore conclude that the observed spectra are not a simple sum of both components, but a reflection of plasmon-exciton interaction of the QD/Au core−satellite HNC system.

To investigate photocatalytic activities and mechanisms of the semiconductor/metal nanosystem, we assembled the as-prepared QD/Au core−satellite HNCs onto GNS to form a well-dispersed and monolayered QD/Au-G nanocomposite (Figure 3a,the typical sizes of the QD/Au-G sample range from 500 nm to 2 $\mu$m) and its photocurrent responses were measured first. For comparison, the precursor QDs, and an equivalent mixture of Au NPs (∼2 nm, see Figure S5 in the Supporting Information) and QD (denoted as QD-Au) were also assembled on the G surface with similar monolayer particle density (Figure 3b, c) for measurements. In the experiments, the transient photocurrent responses of the QD-G, QD-Au-G, and QD/Au-G electrodes were recorded respectively for several on−off cycles of solar irradiation, using $NaNO_3$ (0.1M) solution or mixed solution of $Na_2S$ (0.1 M) and $Na_2SO_3$ (0.02 M) as electrolyte solution to study the transfer process of photogenerated electron and hole in the HNCs. As shown in Figure 3d, e, using either $NaNO_3$ (0.1 M) or $Na_2S$ (0.1 M)+$Na_2SO_3$ (0.02 M) as electrolyte solution, an apparently boosted anodic photocurrent response appears for control QD-G (black line) and QD-Au-G (green line) samples under solar illumination, and the on−off cycles of the photocurrent are reproducible. Because the discrete QDs and AuNPs in control QD-Au-G sample are randomly arranged, the QD-Au-G sample exhibits even lower transient photocurrent than QD-G sample. The response indicates that most of photogenerated electrons transport to the back contact across the sample to produce photocurrent under solar irradiation.[39,40]

The QD/Au-G samples, however, display completely different photocurrent responses when using the aforementioned two different electrolyte solutions. An apparently

boosted cathode photocurrent response was observed when using non-hole scavenger $NaNO_3$ (0.1M) as electrolyte solution (Figure 3d), whereas an apparently boosted anodic photocurrent response (higher than that of QD-G and QD-Au-G samples) appears when using hole scavenger ($Na_2S$ (0.1 M) + $Na_2SO_3$ (0.02 M)) as electrolyte solution (Figure 3e).The different photocurrent responses illustrate that the electric and hole transfer process (or mechanism) of the QD/Au-G system are different, depending on electrolyte solution used. Therefore, we tentatively propose a carrier migration mechanism of the QD/Au-G sample under different conditions, as illustrated in Figure 3f, g. Under visible-light irradiation, electrons (e−) are excited from the VB to the CB of the core QD; meanwhile, the satellite Au NPs can form strong and localized plasmonic near-field to enhance solar absorption and to increase the electron−hole pair generation rate at the surface of semiconductor,[25−27,41−43] and then transfer electrons into satellite Au NPs, which behaving as electron buffer to store electrons, rendering the Fermi level of the composite shifts close to the CB of the semiconductor.[37] Whenin the absence of hole scavenger (Figure 3f), the holes will preferentially transfer to the electrode and lead to cathode photocurrent response as shown in Figure 3d. But when introducing hole scavenger, the photogenerated holes will be consumed by hole scavenger and the electrons preferentially transfer to electrode as shown in Figure 3g, leading to anodic photocurrent response (Figure 3e). For comparison, the photocurrent responses of the graphene-free QD, QD-Au, and QD/Au NPs using $NaNO_3$ (0.1M) as electrolyte solution were also measured (see Figure S6 in the Supporting Information). They all show anodic photocurrent response, and the QD/Au sample also has a highest photocurrent response compared with QD and QD-Au samples, but all lower than their graphene composites, which illustrates that graphene can further enhance the photocatalytic activity of the HNCs. The photocurrent responses showed also a better photocatalytic activity of the QD/Au photocatalyst.

We further explore the QD/Au-G composite for visible-light photocatalytic applications. First, the methylene blue (MB) and Rhodamine B (RDB) photodegradation experiments were carried out using QD/Au-G as phtotocatalysts and QD-G and QD-Au-G with same concentration (in terms of QD particle numbers) as reference catalysts, under visible light ($\lambda$ >420 nm). In the measurement, the normalized temporal concentration changes ($C/C_o$) of MB and RDB during the photodegradation process were proportional to the normalized maximum absorbance ($A/A_o$) and derived from the changes in the dye's absorption profile ($\lambda$ = 660 nm for MB and 550 nm for RDB) at a given time interval. As clearly seen from Figure 4a, b, the QD/Au-G composite showed significant progress in the photodegradation of MB and RDB compared to the reference catalysts of QD-G and QD-Au-G composites. As shown in Figure 4a, after 1 h of continuous irradiation with visible-light, ∼50% and ∼65% of the initial MB were decomposed by the reference QD-Au-G and QD-G catalysts, respectively. Contrastingly, the QD/Au-G HNC catalyst exhibited impressive photodegradation capability, ∼80% of the initial MB were decomposed after 1h of continuous irradiation. For photodegradation of RDB (Figure 4b), after 1h of continuous irradiation with visible light, ∼80% and ∼95% of the initial RDB were decomposed by the reference QD-Au-G and QD-G catalysts, respectively. More impressively, the QD/Au-G HNC catalyst exhibited superb photodegradation capability, almost 100% of the initial RDB were decomposed after 30 min of continuous irradiation. Both of the two dyes cannot be decomposed under visible light illumination in the absence of photocatalytsts. The dye photodegradation experiments proved clearly the plasmon effect and enhancement on photocatalytic activities of the QD/Au-G HNC catalysts. The durability of the QD/Au-G catalysts for the degradation of MB under visible light was also checked (see Figure S9a in the Supporting Information). The photodegradation of MB was monitored for four consecutive cycles, each for 1 h. There was no significant decrease in photodegradation rate during the four consecutive cycles, indicating good stability of the as-prepared QD/Au-G photocatalysts. The photodegradation rate of MB was about 2 times fast compared with that currently reported using $TiO_2$-G (P25-G) composite as high-performance photocatalyst.[44]

Except for excellent performance for dye photodegradation, the as-prepared QD/Au HNC and its graphene composite (QD/Au-G) exhibits also highly efficient performance in photocatalytic $H_2$ production from water containing 0.35 M $Na_2S$ and 0.25 M $Na_2SO_3$. As shown in Figure 4c, d, the QD, QD-Au, and QD/Au NPs can all continue to produce $H_2$ from water at a constant rate for 4 h, and the rate of $H_2$ evolution are 898, 442, and 1307 $\mu$mol $h^{-1}$ $g^{-1}$, respectively. The QD/Au HNCs obviously have a better photocatalytic activity than the QD NPs and QD-Au NPs. And we found experimentally that the size of satellite Au NPs have a great impact on the photocatalytic activity of the QD/Au HNCs. As shown in Figure S7 in the Supporting Information, the nonplasmonic QD/Au HNCs with smaller size (<2 nm) Au NPs (denoted as QD/Au1), due to lack of (or very weak) plasmonic property as confirmed by undetectable dark-field scattering image, showed moderate enhancement in photocatalytic activity for $H_2$ generation (as compared with Au-free QDs) because of improved charge separation and the favorable accumulation of electrons on small Au NPs of the QD/Au systems, whereas the typically prepared plasmonic QD/Au HNCs (∼2 nm Au NPs, denoted as QD/Au2 herein) displayed significantly improved photocatalytic performance in $H_2$ production because of additional plasmonic effect and enhancement. After combining QD/Au HNCs with graphene, the photocatalytic activity was further enhanced because of the unique features of graphene.[14] Although the three samples (QD-G, QD-Au-G, and QD/Au-G) with similar monolayer particle density on G can all continue to produce $H_2$ from water at a constant rate for 4 h, the QD-G composites show good photocatalytic $H_2$ production activity, but the rate of $H_2$ evolution is low (2028 $\mu$mol $h^{-1}$ $g^{-1}$), whereas the QD-Au-G sample show lower photocatalytic $H_2$-production activity compared with the QD-G sample, with the rate of $H_2$ evolution of ∼915 $\mu$mol $h^{-1}$ $g^{-1}$, which may be a reflection of invalid or even counterproductive plasmon-exciton interactions of the system for $H_2$production since the discrete QDs and Au NPs (∼2 nm) in this construction are indirectly contacted and randomly arranged. Very impressively, the photocatalytic $H_2$ production activity of the QD/Au-G sample is markedly enhanced, with the rate of $H_2$ evolution achieving a maximum of 3113 $\mu$mol $h^{-1}$ $g^{-1}$, which is about 155% enhancement compared to nonplasmonic QD-G sample and 340% enhancement compared to control QD-Au-G sample, and the corresponding QE of QD/Au-G catalyst is about 25.4% at 450 nm, which is also higher than most of the graphene-based photocatalysts.[14,19,45]

In our photocatalytic system, the introduction of graphene enhances further $H_2$generation activity of the QD system,

which is mainly due to three reasons:[4,10,36] First, the as-prepared nanocrystals-graphene complexes have good water dispersity because graphene can easily disperse in water,[35] and most of hydrophobic ligands of nanocrystals can be removed by washed them with ethanol, and replaced by $S^{2-}$ from hole scanvenger because $S^{2-}$ ions have stronger bonding with nanocrystals.[46] This is confirmed by the corresponding FT-IR spectra shown in Figure 5, in which both the asymmetric

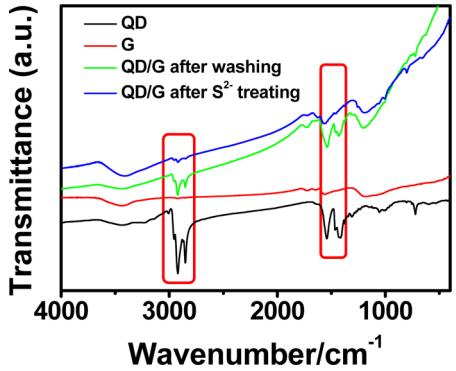


**Figure 5.** FT-IR spectra of oleic acid stabled CdSe/CdS nanocrystals after purification (black), graphene (red), the CdSe/CdS-graphene complexes washed with ethanol three times (green), the CdSe/CdS-graphene complexes dissolved in $Na_2S/Na_2SO_3$for 1 h and washed with water (blue).

vibration band of the-$COO^-$ (1550 $cm^{-1}$) and stretching vibration of C−H (3000−2800 $cm^{-1}$) are noticeably decreased during the processes. As a result, the nanocrystals can directly contact with graphene and the resulting nanocrystal−graphene complexes show good water dispersity, leading to an enhancement of photocatalytic activity as shown in Figure S8 in the Supporting Information. Second, the graphene can serve as an acceptor of the photogenerated electrons from semiconductor nanocrystals and effectively suppress the recombination of the photoexcited electron and hole pairs, leaving more carriers to form reactive sites.[14,45] Third, compared to pure nanocrystals, the graphene has larger specific surface area, offers more active adsorption sites and photocatalytic reaction centers, which can also enhance the photocatalytic activity.[14,45]

The graphene content of QD/Au-G composites have a significant effect on the photocatalytic activity of catalyst, as shown in Figure 6. We found that 1% graphene have a best $H_2$ production results, too much graphene content led to a decrease of the photocatalytic performance. This is reasonable

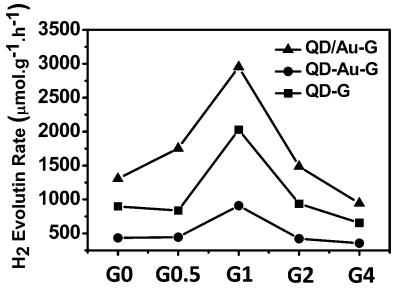


**Figure 6.** Comparison of the visible-light photocatalytic activity of samples QD-G, QD-Au-G, QD/Au-G for the$H_2$ production with different graphene content (0, 0.5, 1, 2, and 4%) using 0.35 M $Na_2S$ and 0.25 M $Na_2SO_3$ aqueous solution as a sacrificial reagent.

because excessive amount of graphene can shield the incident light, which decrease the amount of photogenerated electrons, meanwhile, graphene can cover the active sites of catalyst surface and hinder catalyst contact with hole scavenger.[14,45] More importantly, the QD/Au-G photocatalysts display good photostability (see Figure S9b in the Supporting Information). Both the dye photodegradation and photocatalytic $H_2$ production results proved that the satellite Au NPs of the QD/Au HNCs have a synergistic effect and strong plasmonic enhancement on their photocatalytic activities, making the as-prepared semiconductor/metal HNCs very promising for potential photocatalytic applications.

## 4. CONCLUSION

In summary, we have developed a semiconductor/metal HNC photocatalyst consisting of CdSe/CdS-Au core−satellite HNCs for visible-light dye photodegradation and $H_2$ production from water. The as-synthesized photocatalyst exhibits excellent plasmon-enhanced photocatalytic activities toward both photodegradation of organic dye and visible-light $H_2$ generation from water. The rate of $H_2$ evolution achieves a maximum of 3113 $\mu$mol $h^{-1}$ $g^{-1}$, which is about 155% enhancement compare to nonplasmonic QD-G sample and 340% enhancement compare to control QD-Au-G sample, and its QE is about 25.4%. The enhanced photocatalytic activity rise from the special exciton−plasmon interactions of the semiconductor/metal HNCs. The small satellite Au NPs directly contacted on the surface of CdSe/CdS NCs form a strong and localized electromagnetic energy close to the particle's surfaces, which enhances solar absorption and increases the electron−hole pair generation rate at the surface of the semiconductor QDs. Moreover, combining the HNC photocatalyst with GNS further enhances the photocatalytic activities because GNS possesses an excellent electron transport property and an extremely high specific surface area. This system may provide a good platform for further nanoengineering of this new class of semiconductor/metal HNC system (with size/morphology control, band gap and composition engineering of the semiconductor/metal components) for optimal plasmon-enhanced photocatalytic applications.

## ■ ASSOCIATED CONTENT

### Supporting Information

Additional information includes XPS spectra of GO and G, EDS spectra and the calculated atomic ratio (AT) of the QD/Au HNCs, FDTD simulation of QD/Au HNCs, the absorption and PL spectra of the QDs and QD-Au NPs mixture, the absorption spectrum and TEM image of the control Au NPs used, the photocurrent responses of the QD, QD/Au HNC, QD and Au mixed nanoparticles, the TEM and dark field scatterring images of different size QD/Au HNCs and their $H_2$ production rate, the $H_2$ production rate of the as-prepared QD-G complexes before and after the washing treatment, Cycling runs in the photodegradation of methylene blue and photocatalytic $H_2$ production of QD/Au-G sample. This material is available free of charge via the Internet athttp://pubs.acs.org.

## ■ AUTHOR INFORMATION

### Corresponding Author

*E-mail: ydjin@ciac.ac.cn.

### Notes

The authors declare no competing financial interest.

## ■ ACKNOWLEDGMENTS

The authors acknowledge research support from start-up funds from the Changchun Institute of Applied Chemistry of Chinese Academy of Sciences, the Hundred Talents Program of the Chinese Academy of Sciences, and the State Key Laboratory of Electroanalytical Chemistry (no. 110000R387).

## ■ REFERENCES

(1) Fujishima, A.; Honda, K. Electrochemical Photolysis of Water at a Semiconductor Electrode. *Nature* **1972**, *238*, 37−38.
(2) Hoffmann, M. R.; Martin, S. T.; Choi, W.; Bahnemann, D. W. Environmental Applications of Semiconductor Photocatalysis. *Chem. Rev.* **1995**, *95*, 69−96.
(3) Chen, X. B.; Shen, S. H.; Guo, L. J.; Mao, S. S. Semiconductor-Based Photocatalytic Hydrogen Generation. *Chem. Rev.* **2010**, *110*, 6503−6570.
(4) Xiang, Q. J.; Yu, J. G.; Jaroniec, M. Graphene-Based Semiconductor Photocatalysts. *Chem. Soc. Rev.* **2012**, *41*, 782−796.
(5) Tian, J. Q.; Liu, Q.; Cheng, N. Y.; Asiri, A. M.; Sun, X. P. Self-Supported $Cu_3P$ Nanowire Arrays as an Integrated High-Performance Three-Dimensional Cathode for Generating Hydrogen from Water. *Angew. Chem., Int. Ed.* **2014**, *53*, 9577−9581.
(6) Xing, Z. C.; Liu, Q.; Asiri, A. M.; Sun, X. P. Closely Interconnected Network of Molybdenum Phosphide Nanoparticles: A Highly Efficient Electrocatalyst for Generating Hydrogen from Water. *Adv. Mater.* **2014**, *26*, 5702−5707.
(7) Tian, J. Q.; Liu, Q.; Asiri, A. M.; Sun, X. P. Self-Supported Nanoporous Cobalt Phosphide Nanowire Arrays: An Efficient 3D Hydrogen-Evolving Cathode over the Wide Range of pH 0−14. *J. Am. Chem. Soc.* **2014**, *136*, 7587−759.
(8) Asahi, R.; Morikawa, T.; Ohwaki, T.; Aoki, K.; Taga, Y. Visible-Light Photocatalysis in Nitrogen-Doped Titanium Oxides. *Science* **2001**, *293*, 269−271.
(9) Ni, M.; Leung, M. K. H.; Leung, D. Y. C.; Sumathy, K. A Review and Recent Developments in Photocatalytic Water-Splitting using $TiO_2$ for Hydrogen Production. *Renewable Sustainable Energy Rev.* **2007**, *11*, 401−425.
(10) Daneshvar, N.; Salari, D.; Khataee, A. R. J. Photocatalytic Degradation of Azo Dye Acid Red 14 in Water on ZnO as an Alternative Catalyst to $TiO_2$. *J. Photochem. Photobiol., A* **2004**, *162*, 317−322.
(11) Zou, Z. G.; Ye, J. H.; Sayama, K.; Arakawa, H. Direct Splitting of Water under Visible Light Irradiation with an Oxide Semiconductor Photocatalyst. *Nature* **2001**, *414*, 625−627.
(12) Kudo, A.; Miseki, Y. Heterogeneous Photocatalyst Materials for Water Splitting. *Chem. Soc. Rev.* **2009**, *38*, 253−278.
(13) Zhang, k.; Guo, L. J. Metal Sulphide Semiconductors for Photocatalytic Hydrogen Production. *Catal. Sci. Technol.* **2013**, *3*, 1672−1690.
(14) Li, Q.; Guo, B. D.; Yu, J. G.; Ran, J. R.; Zhang, B. H.; Yan, H. J.; Gong, J. R. Highly Efficient Visible-Light-Driven Photocatalytic Hydrogen Production of CdS-Cluster-Decorated Graphene Nanosheets. *J. Am. Chem. Soc.* **2011**, *133*, 10878−10884.
(15) Han, Z.; Qiu, F.; Eisenberg, R.; Holland, P. L.; Krauss, T. D. Robust Photogeneration of $H_2$ in Water using Semiconductor Nanocrystals and a Nickel Catalyst. *Science* **2012**, *338*, 1321−1324.
(16) Murray, C. B.; Norris, D. J.; Bawendi, M. G. Synthesis and Characterization of Nearly Monodisperse CdE (E = sulfur, selenium, tellurium) Semiconductor Nanocrystallites. *J. Am. Chem. Soc.* **1993**, *115*, 8706−8715.
(17) Peng, X. G.; Manna, L.; Yang, W. D.; Wickham, J.; Scher, E.; Kadavanich, A.; Alivisatos, A. P. Shape Control of CdSe Nanocrystals. *Nature* **2000**, *404*, 59−61.
(18) Norris, D. J.; Efros, A. L.; Erwin, S. C. Doped Nanocrystals. *Science* **2008**, *319*, 1776−1779.
(19) Amirav, L.; Alivisatos, A. P. Photocatalytic Hydrogen Production with Tunable Nanorod Heterostructures. *J. Phys. Chem. Lett.* **2010**, *1*, 1051−1054.
(20) Zhao, Q.; Ji, M. W.; Qian, H. M.; Dai, B. S.; Weng, L.; Gui, J.; Zhang, J. T.; Ouyang, M.; Zhu, H. S. Controlling Structural Symmetry of a Hybrid Nanostructure and its Effect on Efficient Photocatalytic Hydrogen Evolution. *Adv. Mater.* **2014**, *26*, 1387−1392.
(21) Fang, Z.; Wang, Y. B.; Song, J. B.; Sun, Y. M.; Zhou, J. J.; Xu, R.; Duan, H. W. Immobilizing CdS Quantum Dots and Dendritic Pt Nanocrystals on Thiolated Graphene Nanosheets toward Highly Efficient Photocatalytic $H_2$ Evolution. *Nanoscale* **2013**, *5*, 9830−9838.
(22) Xie, G. C.; Zhang, K.; Guo, B. D.; Liu, Q.; Fang, L.; Gong, J. R. Graphene-Based Materials for Hydrogen Generation from Light-Driven Water Splitting. *Adv. Mater.* **2013**, *25*, 3820−3839.
(23) Liu, Q.; Tian, J. Q.; Cui, W.; Jiang, P.; Cheng, N. Y.; Asiri, A. M.; Sun, X. P. Carbon Nanotubes Decorated with CoP Nanocrystals: A Highly Active Non-Noble-Metal Nanohybrid Electrocatalyst for Hydrogen Evolution. *Angew. Chem., Int. Ed.* **2014**, *53*, 6710−6714.
(24) Xie, G. C.; Zhang, K.; Fang, H.; Guo, B. D.; Wang, R. Z.; Yan, H.; Fang, L.; Gong, J. R. A Photoelectrochemical Investigation on the Synergetic Effect between CdS and Reduced Graphene Oxide for Solar-Energy Conversion. *Chem.Asian J.* **2013**, *8*, 2395−2400.
(25) Liu, Z. W.; Hou, W. B.; Pavaskar, P.; Aykol, M.; Cronin, S. B. Plasmon Resonant Enhancement of Photocatalytic Water Splitting under Visible Illumination. *Nano Lett.* **2011**, *11*, 1111−1116.
(26) Ingram, D. B.; Linic, S. Water Splitting on Composite Plasmonic-Metal/Semiconductor Photoelectrodes: Evidence for Selective Plasmon-Induced Formation of Charge Carriers Near the Semiconductor Surface. *J. Am. Chem. Soc.* **2011**, *133*, 5202−5205.
(27) Qu, Y. Q.; Cheng, R.; Su, Q.; Duan, X. F. Plasmonic Enhancements of Photocatalytic Activity of Pt/n-Si/Ag Photodiodes Using Au/Ag Core/Shell Nanorods. *J. Am. Chem. Soc.* **2011**, *133*, 16730−16733.
(28) Li, H. Y.; Liu, S.; Tian, J. Q.; Wang, L.; Lu, W. B.; Luo, Y. L.; Asiri, A. M.; Al-Youbi, A. O.; Sun, X. P. Ternary Nanocomposites of Porphyrin, Angular Au Nanoparticles and Reduced Graphene Oxide: Photocatalytic Synthesis and Enhanced Photocurrent Generation. *ChemCatChem.* **2012**, *4*, 1079−1083.
(29) Li, H. Y.; Wenbo Lu, W. B.; Tian, J. Q.; Luo, Y. L.; Asiri, A. M.; Abdulrahman, O.; Al-Youbi, A. Q.; Sun, X. P. Synthesis and Study of Plasmon-Induced Carrier Behavior at $Ag/TiO_2$ Nanowires. *Chem.—Eur. J.* **2012**, *18*, 8508−8514.
(30) Cheng, N. Y.; Tian, J. Q.; Liu, Q.; Ge, C. J.; Qusti, B. H.; Asiri, A. M.; Al-Youbi, A. Q.; Sun, X. P. Au-Nanoparticle-Loaded Graphitic Carbon Nitride Nanosheets: Green Photocatalytic Synthesis and Application toward the Degradation of Organic Pollutants. *ACS Appl. Mater. Interfaces.* **2013**, *5*, 6815−6819.
(31) Li, J. J.; Wang, Y. A.; Guo, W. Z.; Keay, J. C.; Mishima, T. D.; Johnson, M. B.; Peng, X. G. Large-Scale Synthesis of Nearly Monodisperse CdSe/CdSCore/Shell Nanocrystals using Air-Stable Reagents via Successive Ion Layer Adsorption and Reaction. *J. Am. Chem. Soc.* **2003**, *125*, 12567−12575.
(32) Peng, X. G.; Schlamp, M. C.; Kadavanich, A. V.; Alivisatos, A. P. Epitaxial Growth of Highly Luminescent CdSe/CdS Core/Shell Nanocrystals with Photostability and Electronic Accessibility. *J. Am. Chem. Soc.* **1997**, *119*, 7019−7029.
(33) Thibert, A.; Frame, F. A.; Busby, E.; Holmes, M. A.; Osterloh, F. E.; Larsen, D. S. Sequestering High-Energy Electrons to Facilitate Photocatalytic Hydrogen Generation in CdSe/CdS Nanocrystals. *J. Phys. Chem. Lett.* **2011**, *2*, 2688−2694.
(34) Yang, J.; Ying, J. Y. A General Phase-Transfer Protocol for Metal Ions and its Application in Nanocrystal Synthesis. *Nat. Mater.* **2009**, *8*, 683−689.
(35) Ai, K. L.; Liu, Y. L.; Lu, L. H.; Cheng, X. L.; Huo, L. H. A Novel Strategy for Making Soluble Reduced Graphene Oxide Sheets Cheaply by Adopting an Endogenous Reducing Agent. *J. Mater. Chem.* **2011**, *21*, 3365−3370.
(36) Guo, S. J.; Sun, S. H. FePt Nanoparticles Assembled on Graphene as Enhanced Catalyst for Oxygen Reduction Reaction. *J. Am. Chem. Soc.* **2012**, *134*, 2492−2495.

(37) Subramanian, V.; Wolf, E. E.; Kamat, P. V. Catalysis with $TiO_2$/Gold Nanocomposites. Effect of Metal Particle Size on the Fermi Level Equilibration. *J. Am. Chem. Soc.* **2004**, *126*, 4943−4950.
(38) Jin, Y. D.; Gao, X. H. Plasmonic Fluorescent Quantum Dots. *Nat. Nanotechnol.* **2009**, *4*, 571−576.
(39) Xu, Z. H.; Yu, J. G. Visible-Light-Induced Photoelectrochemical Behaviors of Fe-Modified $TiO_2$ Nanotube Arrays. *Nanoscale* **2011**, *3*, 3138−3144.
(40) Yu, J. G.; Dai, G. P.; Huang, B. B. Fabrication and Characterization of Visible-Light-Driven Plasmonic Photocatalyst Ag/AgCl/$TiO_2$ Nanotube-Arrays. *J. Phys. Chem. C* **2009**, *113*, 16394−16401.
(41) Schaadt, D. M.; Feng, B.; Yu, E. T. Enhanced Semiconductor Optical Absorption via Surface Plasmon Excitation in Metal Nanoparticles. *Appl. Phys. Lett.* **2005**, *86*, 063106.
(42) Atwater, H. A.; Polman, A. Plasmonics for Improved Photovoltaic Devices. *Nat. Mater.* **2010**, *9*, 205−213.
(43) Ferry, V. E.; Sweatlock, L. A.; Pacifici, D.; Atwater, H. A. Plasmonic Nanostructure Design for Efficient Light Coupling into Solar Cells. *Nano Lett.* **2008**, *8*, 4391−4397.
(44) Zhang, H.; Lv, X. J.; Li, Y. M.; Wang, Y.; Li, J. H.P25-Graphene Composite as a High Performance Photocatalyst. *ACS Nano* **2010**, *4*, 380−386.
(45) Zhang, J.; Yu, J. G.; Jaroniec, M.; Gong, J. R. Noble Metal-Free Reduced Graphene Oxide-$Zn_xCd_{1-x}S$ Nanocomposite with Enhanced Solar Photocatalytic $H_2$-Production Performance. *Nano Lett.* **2012**, *12*, 4584−4589.
(46) Ithurria, S.; Talapin, D. V. Colloidal Atomic Layer Deposition (c-ALD) using Self-Limiting Reactions at Nanocrystal Surface Coupled to Phase Transfer between Polar and Nonpolar Media. *J. Am. Chem. Soc.* **2012**, *134*, 18585−18590.